Verifying Strand Transposition in Stator Windings via X-ray Computed Tomography derived Three-Dimensional Models

Hoole, J., North, D., Simpson, N., Mellor, P. H.

ACCEPTED PAPER

Presented at the 6th IEEE Workshop on Electrical Machines Design, Control and Diagnosis (WEMDCD) April 2023

DOI: 10.1109/WEMDCD55819.2023.10110906

Verifying Strand Transposition in Stator Windings via X-ray Computed Tomography derived Three-Dimensional Models

Joshua Hoole
Electrical Energy Management Group
University of Bristol
Bristol, United Kingdom
josh.hoole@bristol.ac.uk

Dominic North
Electrical Energy Management Group
University of Bristol
Bristol, United Kingdom
dj.north@bristol.ac.uk

Nick Simpson
Electrical Energy Management Group
University of Bristol
Bristol, United Kingdom
nick.simpson@bristol.ac.uk

Philip H. Mellor
Electrical Energy Management Group
University of Bristol
Bristol, United Kingdom
p.h.mellor@bristol.ac.uk

***Abstract*—To minimise AC losses in power dense electrical machines, multistrand stator windings are routinely employed. However, the magnitude of AC losses can be highly sensitive to the strand transposition achieved in the as-manufactured winding, which can differ significantly from that assumed during design. This paper employs X-ray Computed Tomography (XCT) to verify the twisted strand transposition in a compressed aluminium coil, through the construction of 3D models for each of the strands within the coil. These models enable the strand transposition to be verified by qualitative and quantitative means, providing initial insight into the actual strand transposition achieved at the mid-point of the coil active length.**

***Index Terms*—computed tomography, strand transposition**

I. Introduction

The adoption of power-dense electrical machines with excitation frequencies exceeding 1kHz for automotive and aerospace applications has led to increasing investigation into the variability present in AC losses within multistrand stator windings [1], [2]. While multistrand configurations are used to mitigate skin effect losses, proximity and bundle-level losses can be exacerbated due to the as-manufactured strand transposition, especially in random windings [3].

Prior work has defined various idealised strand transpositions, and these are routinely assumed during the design and analysis of electrical machine windings [4], [5]. To date however, there have been limited studies into the characterisation of strand transposition in as-manufactured windings, and the identification of complete three-dimensional strand paths around a coil has yet to be performed [6]. Consequently, for coil winding technologies that result in significant mechanical strand-to-strand and strand-to-tool interactions (such as random windings [5] and compressed coils [7]), existing AC loss estimation methods do not adequately account for the actual strand transposition achieved during manufacture.

If the strand distribution can be established by non-destructive means, rather than through sectioning [8] or simulations [9], then a set of representative windings, produced by a specific manufacturing method can be studied and statistically evaluated to give insight on the expected bounds and distribution of winding loss. Such data could then be used to improve confidence in batch consistency or inform improved modelling and manufacturing practices. This paper will demonstrate the use of X-ray Computed Tomography (XCT) and image processing methods to verify the strand transposition achieved in an as-manufactured compressed aluminium coil. Qualitative and quantitative means are used to characterise the strand transposition, along with a discussion on the wider exploitation and challenges of XCT-derived 3D models of stator windings.

II. Compressed Multistrand Aluminium Coils

Compressed aluminium coils have been proposed as a method to increase fill factors and reduce mass in power-dense electrical machines [1], [8]. This paper considers the coil shown in Fig. 1, consisting of 10 turns of 8 parallel 'strands-in-hand'. The manufacturing process to achieve a 70% fill factor has been described previously [10]. Continuity tests of each coil strand showed no fractures occurred during manufacture.

Prior to coil winding and compression, the 8 parallel strands were twisted to achieve a uniform strand transposition throughout the winding to reduce the AC losses of the multistrand configuration [10]. Pre-twisting of the wire was proposed as an alternative to high-cost to Litz windings, which can also present manufacturing challenges [11], and to improve the conductor fill. As a result of the adoption of the pre-twisting method, the achieved strand transposition in the manufactured

The authors acknowledge the University of Sheffield Tomography Centre (STC) funding from EPSRC (EP/T006390/1).

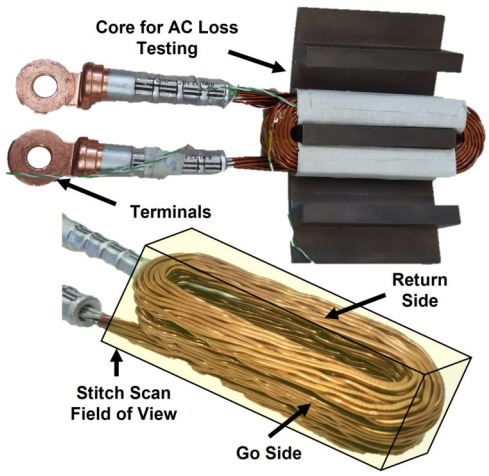

Fig. 1. Compressed multistrand aluminium coil

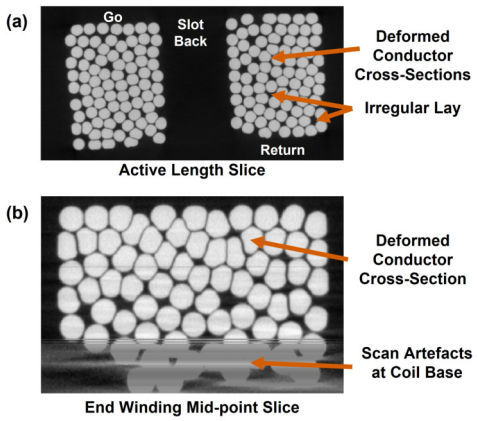

Fig. 2. Example XCT slices of a) the active length and b) end winding cross-section

coil must be verified in order to validate the assumptions used during modelling of the coil. Whilst a prototype coil has been available for AC loss testing, the cost associated with future design cycles could be reduced through better representing the achieved strand transposition within modelling approaches.

A. X-Ray Computed Tomography

Within XCT, repeated 2D X-ray projections of an object are taken from different orientations, to generate a 3D model of the object and internal structures [6]. As a result, XCT provided a method to see *within* the compressed coil structure to support the verification of the achieved strand transposition.

Previous work by the authors performed an XCT scan in which the field of view encompassed half of the coil active length and one end winding [6]. In order to verify the strand transposition, the full coil would need to be scanned to enable each of the 8 parallel strands to be traced throughout the coil.

To scan the full coil, a 'stitch' scan was performed using a Zeiss Xradia Versa 620 X-ray Microscope. Within a stitch scan, multiple XCT scans are performed focusing on different regions of the object, which are then combined into a single dataset. To scan the full coil, 5 individual XCT scans were required, divided along the active length direction of the coil. Each scan achieved a resolution defined by a voxel (i.e. a 3D volumetric pixel) size of 47μm at a tube voltage of 100kV, 1 second exposure and a magnification of 0.4x. Approximately 7 hours of scan time was required for the complete coil. Reconstruction of the X-ray projection resulted in XCT 'slices' and example slices are shown in Fig. 2, in which strand deformation throughout the coil can be observed.

III. Volume Segmentation Process

The output of the XCT scan is the stack of image slices, which is the 3D voxel representation of the coil geometry. It is important to note that within this representation, all voxels are independent to one another and volume segmentation methods are required to link each voxel within the 3D space to individual objects (e.g. strands) within the coil geometry.

While manual segmentation is an option, whereby a user would highlight each pixel in each XCT slice associated with a given object (e.g. a conductor cross-section), for a compressed coil consisting of up to 160 conductor cross-sections over 2,000 XCT slices, automatic and semi-automatic volume segmentation methods are required.

For the compressed coil XCT stack, the MATLAB® Image Processing Toolbox™ was used to perform volume segmentation. Volume segmentation is achieved through identifying changes in the image greyscale intensity, or boundaries in a binary image, as edges of an object. As the multistrand coil XCT volume comprises of a large number of objects of near-identical density, additional image processing as detailed previously and as shown in Fig. 3 was required [6].

For the active length of the coil, where the conductor cross-section shapes and position only vary by limited amounts slice-to-slice, volume segmentation was successfully performed through connecting voxels in each contiguous area across an individual slice, as well as between adjacent slices in the XCT stack. However, it was found in some areas of the active length two strands would be incorrectly joined following segmentation along with incorrect segmentation within the end winding region due to the complexity of the strand paths.

Consequently, the coil was divided into the sub-volumes shown in Fig. 4, each separated by a specific XCT slice. To enhance the volume segmentation in the end windings and incorrectly segmented active length sections, watershed segmentation was employed across the sub-volumes. The watershed process segments images and volumes through identifying greyscale intensity 'ridgelines' and uses these as the boundary between objects [12]. Such an approach however, can lead to over-segmentation, where individual objects are segmented into sub-objects and Fig. 5 provides a visual comparison between XCT slices segmented via contiguous binary regions and the watershed approach. It can also be observed from Fig. 5b that the watershed approach can also lead to the obliteration of conductor cross-sections, along with an increase in computational memory requirements and the

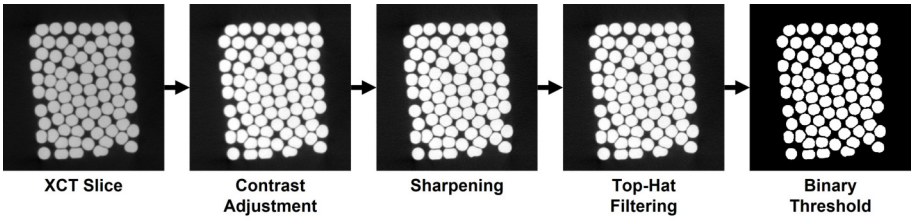

Fig. 3. The XCT slice processing required prior to volume segmentation

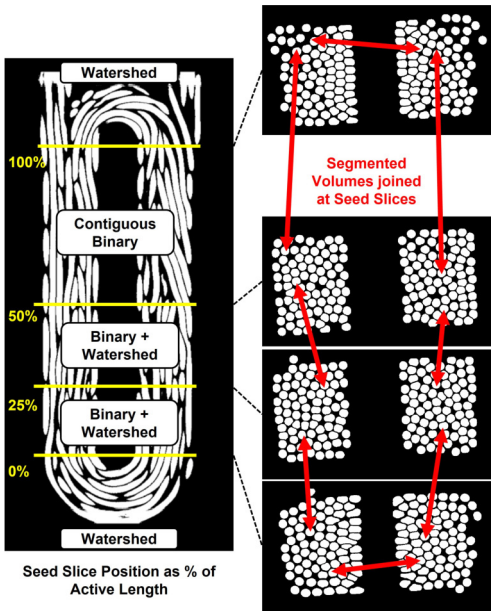

Fig. 4. Definition of XCT seed slices for strand tracing

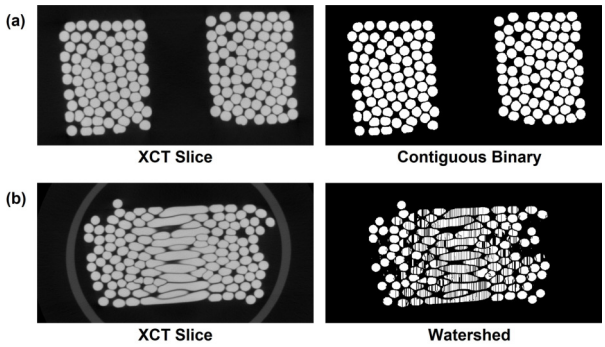

Fig. 5. a) contiguous binary segmentation in the active length and b) watershed segmentation in the end winding

impact of this is discussed in Section V. The 5 sub-volume positions shown in Fig. 4 are therefore a result of minimising the computational expense of processing the large number of sub-objects, along with targeting the segmentation strategy to the characteristics of each sub-volume.

In order to perform volume segmentation in the sub-volumes requiring watershed segmentation, the semi-automatic procedure developed previously was employed [6]. Within this process, the conductor 'seed' positions within the slice at the sub-volume boundary, along with the expected strand path defined as a vector, are used to find the watershed volumes associated with a strand. The closest watershed volume that is penetrated by the search vector is assumed to belong to the current strand. The process is semi-automatic as it proposes the next most likely watershed volume to the user, who can then accept the current volume, or state an alternative [6].

A. Strand Tracing Procedure

Application of the binary contiguous and watershed segmentation approaches resulted in the extraction of 648 volumes across the coil geometry. The next phase of the volume segmentation process was to associate each of these segmented volumes to one of the 8 strands within the coil. This was achieved through using the 'seed' XCT slices that lay between each of the sub-volumes. Through identifying the pair of segmented volumes associated with each conductor cross-section for the seed slice, links between the segmented volumes could be automatically grouped until complete strands were formed. This resulted in each strand being defined by the voxels contained within 81 independent segmented volumes.

IV. Three-Dimensional Strand and Coil Models

The output of the XCT and volume segmentation permitted a 3D model of the coil to be constructed. Fig. 6a shows the 3D rendering of the coil. It is important to note however that the 3D render is based purely on the greyscale intensity values of the original XCT scan stack and therefore provides no information regarding the strand transposition within the coil.

Of more utility within future studies (see Section V), are the 3D models consisting of the grouped segmented volumes for each strand. As these models list all of the voxels associated with each of the 8 strands within the winding, they can be used as a proxy for where the strand path exists in 3D space and hence define the 3D geometry of each individual strand when paired with the known voxel size of 47μm.

A 3D model of an individual strand is shown in Fig. 6b, along with the position of the strand relative to the point cloud of segmented volume centroids in Fig. 6c. The complex strand path can be clearly observed in Fig. 6c. The 8 individual strand 3D models are combined to produce a 3D model of the compressed coil, as shown in Fig. 7, which replicates both the strand path and how the conductor cross-section varies along the stand length due to deformation during manufacture.

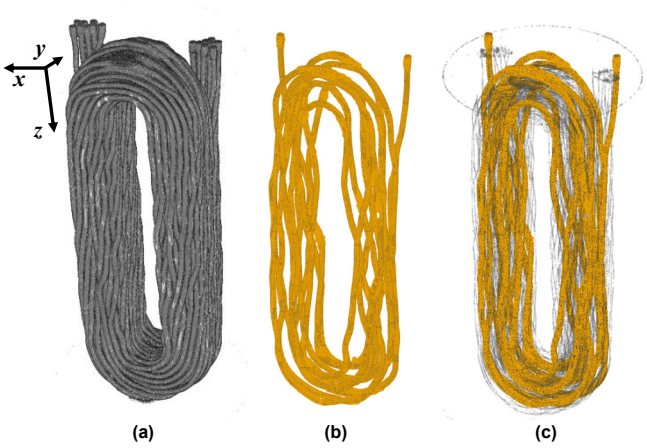

Fig. 6. a) 3D rendering of coil, b) 3D model of a strand and c) 3D strand model with segmented volume centroids

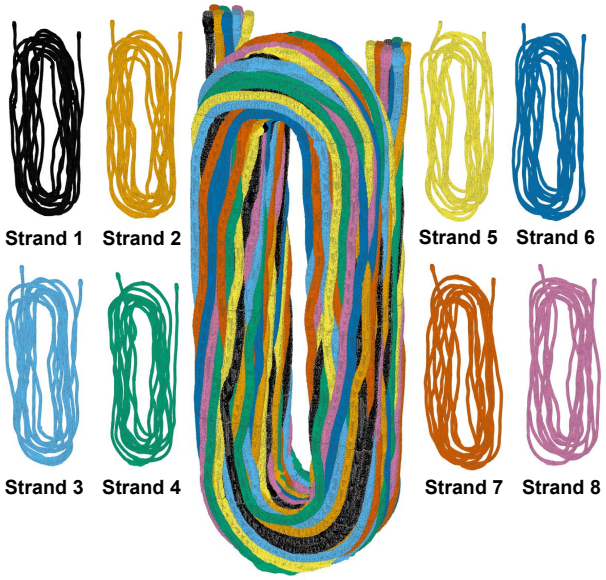

Fig. 7. 3D strand and coil models

A. Verification of Strand Transposition

Upon generation of the 3D models for each of the 8 strands, verification of the target twisted strand transposition could be performed. From visual inspection of the coil, 3D rendering and models shown in Fig. 6a and 7 respectively, twisting of the strands is evident on the surface of the coil. However, the vast majority of the strand transposition will be present in the coil interior, and it is not clear to what extent the compression of the coil during manufacture could have disturbed the strand transposition. Regarding the strand transposition within the coil, Fig. 8 shows 2 strands and the twisting transposition of the strands can be seen throughout the coil.

It was proposed that the strand transposition could be verified in a quantitative manner through computing the centre of mass position for each strand, and comparing these values to a datum of the coil's overall centre of mass. The centre of mass for each strand could be estimated using the average position of the voxels that form each segmented volume associated with a given strand, and the centre of mass position was defined in the following three directions (see Fig. 6a):

- x - positive left to right across the slot width
- y - positive from slot opening to slot back
- z - positive away from terminals along the active length

The deviation in the strand centre of mass position with respect to the coil centre of mass is given in Table I. These values are stated as a percentage of the coil dimension with which they are aligned (e.g. y is relative to the coil slot depth).

As can be observed from Table I, the majority of strands demonstrate centre of mass positions that are within 1% of the overall coil centre of mass. Whilst the values related to an idealised strand transposition would be challenging to define due to the coupling of the strand transposition and the compression of the coil, the values presented in Table I could provide a benchmark for future manufacturing studies.

Table I suggests that Strand 4 lies closer to the slot opening than the other strands due to the larger negative value, poten-

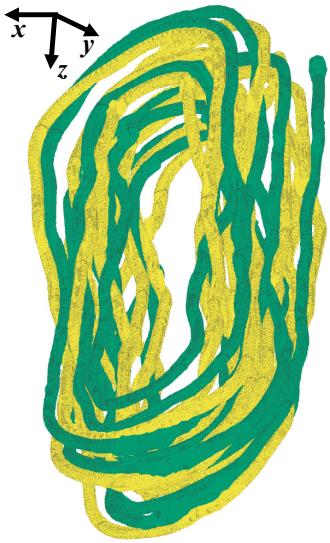

Fig. 8. Evidence of twisted strand transposition between Strands 4 and 5

TABLE I
STRAND CENTRE OF MASS DEVIATION

Strand	Centre of Mass % of Coil Dimension		
	x	y	z
1	-2.5	0.7	0.2
2	-1.9	0.9	0.1
3	1.0	0.9	-0.2
4	0.6	-2.2	-0.1
5	0.4	-0.7	-0.4
6	0.6	0.3	0.7
7	1.0	-0.6	0.0
8	0.9	0.8	-0.1

tially leading to increased AC losses within this strand due to increased flux linkage at the slot opening [4]. Table I also suggests that Strands 1 and 2 tend towards the 'left' hand side of the coil when looking towards the terminal end.

B. Strand and Turn Identification in Active Length

To further characterise the strand transposition achieved within the coil, the strand transposition at the active length mid-point, with reference to the XCT slice at this location, was defined. As the mid-point of the active length aligned with a 'seed' XCT slice used during construction of the 3D models, the strand transposition across the slot depths for the 'go' and 'return' side could be easily identified from the segmented volume pairing performed in Section III-A. The resulting strand transposition is shown in Fig. 9, where the colours and numbers identify which of the 8 parallel strands that the conductor cross-section relates to. Qualitatively, it can be observed that strands are well dispersed across the slot depths. Of note from Fig. 9 is the clustering of Strand 4 turns towards the slot opening, and the close position of two turns of Strand 1 to the left hand side of the slot depths. Both of these observations support the results shown in Table I.

From super-imposing each strand 3D model onto the mid-active length seed XCT slice (see Fig. 10), the turn number associated with each conductor cross-section could also be identified, through tracing the path of the strand from terminal to terminal and progressively labelling each conductor cross-section. The resulting strand turn assignment is shown in Fig. 11 where the colour represents the strand number and numbers represent the turn. The grouping of turn bundles is further highlighted in Fig. 12, where some turns are observed to conform to the original twisted bundle shape (i.e. Turns 1 and 10), whilst others have been flattened across the slot depth during compression, such as Turns 2, 3 and 6. Such information could support voltage stress analysis [13], [14].

V. Use and Challenges of XCT Derived Models

The most evident exploitation opportunity for the strand and turn assignments derived from 3D models is the use of such information in the modelling of multistrand windings that are subject to variable conductor lays. For example, knowledge of the typical conductor lays and strand paths in coils of a given manufacturing process can improve existing 2D Finite Element Analysis (FEA) estimates of AC losses as previously described by the authors [5].

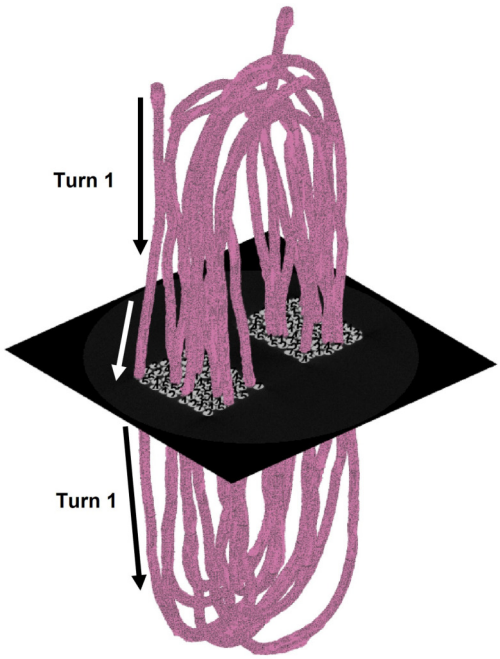

Fig. 10. Turn tracing procedure (Strand 8 shown)

A 2D FEA model was constructed to establish how AC loss modelling practices could be enhanced for future design cycles without relying on physical prototypes. Using the dedicated FEA methodology previously defined [6], it was found that the AC to DC loss ratio at 1.2kHZ was $K_{AC} = 1.8$ for both the go and return slots shown in Fig. 9. An alternative approach for modelling even strand distributions due to twisting is to randomly allocate the strand turns to the conductor cross-sections [6]. However, a 500-iteration Monte Carlo Simulation produced a mean value of $K_{AC} = 2.8$ and 2.7 for the go and return slots respectively and $K_{AC} = 1.8$ lies below the 5$^{\text{th}}$ per-

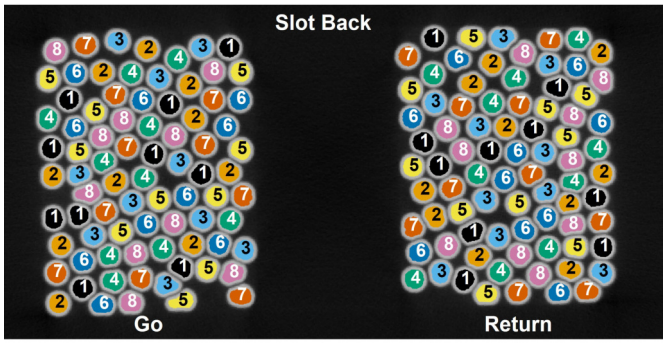

Fig. 9. Identified strand transposition at mid-active length

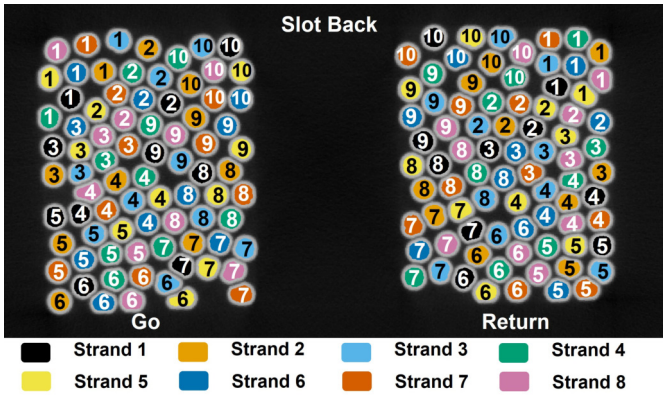

Fig. 11. Identified turn positions at mid-active length

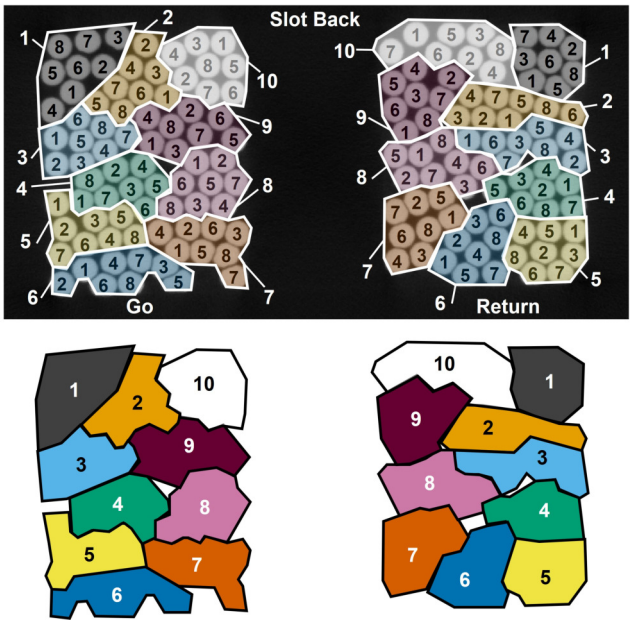

Fig. 12. Identified turn bundles at mid-active length

centile of the estimated AC loss variability. This demonstrates the importance of accurately modelling conductor positions during design to account for the AC loss reduction provided by the twisted strand transposition. These results reinforce the need to verify strand transpositions achieved by manufacture to ensure representative AC loss estimates.

A study into how AC loss estimates vary along the active length with the strand transposition could also be performed through constructing 2D models at various slices along the active length, from which the strand and turn assignment is then populated from the 3D models. However, the 3D models do not currently present a robust method for identifying the strand transposition at an arbitrary location. This is due to voids forming on the 3D model interior during volume segmentation. This could be overcome by extracting surface points of the existing models and re-generating the 3D geometry, however such an approach would require a significant computational memory not available for the current paper (>16GB RAM).

Finally, the generation of 3D models from the XCT data could permit 3D FEA of the actual winding geometry to be performed through discretisation of the geometry into an FEA mesh. Such 3D models would be able to accurately account for the varying strand conductor cross-sections and transposition within the compressed winding. In addition, the accurate modelling of end winding inductance is key to accurate electromagnetic FEA estimations and consequently, the XCT derived 3D models could permit the accurate modelling of end winding geometries, similar to Winterborne et al. [15].

VI. Conclusion

Significant assumptions are currently required during the design of power-dense multistrand windings, both in random and compressed coil configurations. X-ray Computed Tomography (XCT) provides a route to characterising the internal structures of electric machine windings and this paper demonstrated the generation of 3D models for each of the strands in a multistrand compressed aluminium coil. Beyond verifying the strand transposition in the compressed aluminium coil considered within this study, it is anticipated that the workflow presented within this paper will support future advancements in the 3D design, modelling and optimisation of high fill and low loss multistrand stator windings.

Acknowledgment

The authors acknowledge the University of Sheffield Tomography Centre (STC) funding from EPSRC (EP/T006390/1). The authors thank Dr Ria Mitchell for performing the XCT scans at the STC.

References

[1] J. D. Widmer, R. Martin, and B. C. Mecrow, "Precompressed and Stranded Aluminum Motor Windings for Traction Motors," IEEE Trans. Ind. Appl., vol. 52, no. 3, pp. 2215–2223, 2016.

[2] M. Halwas, F. Wirth, and J. Fleischer, "Investigation of the Forming Behaviour of Copper Wires for the Compaction of Windings for Electric Machines," Key. Eng. Mater., vol. 926, pp. 1809–1818, 2022.

[3] P. Mellor, J. Hoole, and N. Simpson, "Computationally efficient prediction of statistical variance in the AC losses of multi-stranded windings," 2021 IEEE Energy Conversion Congress and Exposition (ECCE), pp. 3887–3894, 2021.

[4] A. Bardalai, et al., "Reduction of Winding AC Losses by Accurate Conductor Placement in High Frequency Electrical Machines," IEEE Trans. Ind. Appl., vol. 56, no. 1, pp. 183–193, 2020.

[5] J. Hoole, P. H. Mellor, and N. Simpson, "Designing for Conductor Lay and AC Loss Variability in Multistrand Stator Windings," IEEE Trans. Ind. Appl., vol. 59, no. 2, pp. 1394–1404, 2023.

[6] J. Hoole, R. L. Mitchell, D. North, N. Simpson, and P. H. Mellor, "Characterisation of Compressed Windings via High Resolution X-ray Computed Tomography and Semi-Automatic Segmentation," 48th Annual Conference of the IEEE Industrial Electronics Society (IECON), 2022.

[7] D. Sossong, and I. Brown, "Spaced Orthocyclic Winding Pattern for Improved Die Compressed Coils," 2022 IEEE Energy Conversion Congress and Exposition (ECCE), 2022.

[8] M. C. Kulan, and N. J. Baker, "Life-time characteristics of random wound compressed stator windings under thermal stress," IET Electr. Power Appl., vol. 13, no. 9, pp. 1287–1297, 2019.

[9] M. C. Kulan, N. J. Baker, and J. D. Widmer, "Design and Analysis of Compressed Windings for a Permanent Magnet Integrated Stater Generator," IEEE Trans. Ind. Appl., vol. 53, no. 4, pp. 3371–3378, 2017.

[10] D. North, J. Hoole, N. Simpson, and P. Mellor, "Test Metrics and Damage Fingerprints in Multistranded Compressed Aluminium Windings," 2021 IEEE Energy Conversion Congress and Exposition (ECCE), pp. 3789–3796, 2021.

[11] H. C. Born, et al., "Development of a Production Process for Formed Litz Wire Stator Windings," 12th International Electric Drives Production Conference (EDPC), 2022.

[12] R. Gonzalez, and R. Woods, Digital Image Processing, 4th Ed., Pearson Education Ltd., 2017.

[13] Y. Xie, J. Zhang, F. Leonardo, A. R. Munoz, M. W. Degner, and F. Liang, "Modelling and Verification of Electrical Stress in Inverter-Driven Electric Machine Windings," in IEEE Trans. Ind. Appl., vol. 55, no. 6, pp. 5818–5829, 2019.

[14] A. Hoffmann, B. Knebusch, J. O. Stockbrügger, J. Dittmann, and B. Ponick, "High-Frequency Analysis of Electrical Machines Using Probability Density Functions for an Automated Conductor Placement of Random-Wound Windings," 2021 IEEE International Electric Machines & Drives Conference (IEMDC), 2021.

[15] D. Winterborne, S. Jordan, L. Sjöberg, and G. Atkinson, "Estimation of AC copper loss in electrical machine windings with consideration of end effects," 2020 International Conference on Electrical Machines (ICEM), pp. 847–853, 2020.